Desalination and Water Treatment
www.deswater.com

doi: 10.5004/dwt.2021.27273

227 (2021) 42–57
July

A novel synthesis of quaternary nanocomposite as a potential adsorbent for removal organic pollutants (benzene and toluene) from produced water

Hager R. Ali[a], Rasha S. Mohamed[b], Mahmoud F. Mubarak[c,*], Abeer El Shahawy[d,*]

[a]*Analysis and Evaluation Department, Egyptian Petroleum Research Institute (EPRI), 1 Ahmed El-Zomer St., Nasr City, (11727), Cairo, Egypt, emails: d_hager80@epri.sci.eg (H.R. Ali).*
[b]*Refining Division, Catalysis Department, Egyptian Petroleum Research Institute (EPRI), 1 Ahmed El-Zomer St., Nasr City, (11727), Cairo, Egypt, emails: rashaepri2009@yahoo.com/rashaepri2009@epri.sci.eg*
[c]*Petroleum Applications Department, Egyptian Petroleum Research Institute (EPRI), 1 Ahmed El-Zomer St., Nasr City, (11727), Cairo, Egypt, emails: amrshehata@epri.sci.eg/fathy8753@yahoo.com*
[d]*Department of Civil Engineering, Faculty of Engineering, Suez Canal University, P.O. Box: 41522, Ismailia, Egypt, email: abeer_shahawi@eng.suez.edu.eg*

Received 6 November 2020; Accepted 24 March 2021

ABSTRACT

This paper presents an experimental study on the fabrication and testing of quaternary nanocomposite MCM-41/SBA-15@ACTF/ZIF-8 as an adsorbent to remove benzene and toluene from the produced water. To the best of our knowledge, this nanocomposite is novel. Any research group has not investigated it. The ZIF-8, a nanostructure with amorphous carbon thin film (ACTF), and the mesoporous silica order (MCM-41, SBA-15) were also synthesized in the present study. The incorporation of silica and ACTF synthesized the quaternary composite into the ZIF-8. All adsorbing materials have been evaluated by measuring the water adsorption uptake and characterizing the surface using X-ray photoelectron spectroscopy, Fourier-transform infrared spectroscopy, transmission electron microscopy, and scanning electron microscopy images. It was found that the adsorption rate constants of the quaternary nanocomposite (MCM-41/SBA-15@ACTF/ZIF-8) were 0.494 and 0.413 g/g min for benzene and toluene, respectively. Additionally, the adsorption rates measured in a batch reactor under a wide range of operating conditions were found to agree very well with the homogeneous surface diffusion model with a surface diffusion coefficient that increases exponentially with surface concentration. This indicates that the hydrodynamics effects in the liquid phase of the external mass transfer coefficient have been considered. Besides the batch study, continuous flow columns have been investigated. The breakthrough curves were obtained by varying the flow rate (3, 6 and 9 mL/min), the initial concentration (520, 500, and 1,000 mg/L), and the bed height (3.5, 5.5, and 11 mm). It was found that; the optimum conditions occurred at a low flow rate (3 mL/min), of initial concentration (250 mg/L), and considerable bed height (3.5 mm). The batch and continuous flow column results were evaluated using the isotherm models, which indicated that the continuous flow column study is more preferred than the batch treatment. In continuous adsorption, the benzene and toluene was effectively removed at low benzene and toluene all influent concentration, low flow rate, and high bed depth. The experimental data were consistent with the Thomas model. The high physicochemical pollutants in the wastewater were successfully treated in batch and fixed-bed systems to fall within the WHO permissible concentrations. Also, it was concluded that the Bohart–Adams model successfully predicted toluene desorption rates in the aqueous phase under various operating conditions after accounting for irreversible adsorption using toluene transport parameters estimated from the adsorption studies.

Keywords: Quaternary nanocomposite; Water treatment; Amorphous carbon thin film nanostructure; Petroleum hydrocarbons; Volatile organic compounds

* Corresponding authors.

1. Introduction

Produced water is the largest waste stream in the oil and gas exploration and production processes [1,2]. The produced water problem contains high concentrations of pollutants such as benzene, toluene, ethylbenzene, and xylenes (BTEX) [3,4]. Benzene and toluene can enter the groundwater through leakage from the storage tanks, pipes, and improper burial sites [5]. These pollutants are moderately soluble in seawater, highly volatile, and biodegrade rapidly in the water environment. Consequently, they may cause severe environmental problems [5]. Besides, due to health effects, they are considered high-risk compounds [6]. For example, toluene is suspected of disrupting the central nervous system and is classified as a Group E carcinogen [7]. For these reasons, the EPA has restricted the maximum concentrations of benzene and toluene in drinking water to 5 and 2 μg/L, respectively [8]. It is worth mentioning that the produced water can be disposed through reinjection into the reservoir. However, due to environmental considerations and cost, the surface discharge may be cost-effective compared to reinjection [9,10]. Subsequently, in arrange to comply with the strict legislation, the removal of BTX from water and squander water is essential. Several treatment methods can be used but the efficiency of the treatment processes adopted in these methods is affected by many factors such as oxidation process, extraction, stripping, membranes and biological treatment. On the contrary, adsorption is more effective technique compared to these methods. Additionally, most of these methods have some drawbacks such as high operation cost, high investment and disposal of metal sludge. Therefore, efforts have been made to develop cheap materials for removing pollutants from the aquatic environment.

The advances in materials science and fabrication technology resulted in materials with well-ordered mesoporous structures. Researchers recommended these materials for pollutants removal due to their high surface area, uniform pore size distribution, and tunable pore structure. Thus, they are promising adsorbents for environmentally hazardous compounds [11,12]. Two typical mesoporous silica are reported in reference [13–15]: (i) MCM-41 with long-range ordering giving rise to one-dimensional (1D) mesoporous channels, (ii) SBA-15 with a 2D hexagonal array of mesopore–micropore coexisting pore structures. It was found that they exhibit high thermal stability, high surface area and porosity, and good adsorption performance for volatile organic compounds (VOCs), as reported by [16]. Previous studies have indicated that order mesoporous silica with bimodal pore size distribution (SBA-15) and mesopores order of MCM-41 has a high affinity for adsorbing various VOCs from produced water [17] due to their complementary micropores, which are favorable to the diffusion process [18–21].

Metal-organic frameworks (MOFs) are an advanced class of porous materials that have received attention because of their simple synthesis, excellent porosity, and facile modification [22]. Various attempts have been made to increase the efficiency of MOFs, including the incorporation of other components to form MOF composites [23]. A recent trend is to furnish functional composite of the MOFs or coordination compounds by hybridizing them with different active species like metal nanoparticles, oxides, polymers, graphene and graphene oxide, carbon nanotubes, amorphous carbon thin film nanostructure (ACTF) and mesoporous silica [24–29]. Then, the fabrication of MOFs/silica composites could impart the MOFs with many advantages: improving the water dispersibility, strengthening the stability, and enhancing the mechanical properties [30,31]. Thus, mesoporous silica such as MCM-41 and SBA-15 have been reported as supports in MOF synthesis, as an effort to increase the pore size of MOF and to reduce diffusion problems when used as adsorbents [32]. Silica has a leading impact on the production of MOF crystals and can efficiently plan and handle MOF morphology. The interaction between silanol groups on the precursor and metal center of the silica may cause structural modification and increase surface area and the volume of micropore, which encourages the application of adsorption [33,34].

Yan et al. [35] successfully synthesized ZIF-8/silica composite in the presence of a swelling agent as an adsorbent for removing phthalic acid, zeolite imidazolate frameworks (ZIFs), a sub-family of imidazolate ligand-composed MOFs, due to their superior thermal and chemical properties. The function of the swelling agent was in the expansion of the composite pore. In this study, the removal of volatile organic compounds (benzene and toluene) from produced water was carried out using synthesized novel quaternary nanocomposites adsorbent (MCM-41-SBA-15@ACTF-ZIF-8). The authors of the current study believe that the mesopores of carbon silicate materials, MOF particles can ideally be immobilized into the silicates, and the resulting composite nanostructure would exhibit characteristics of both components. The result revealed that MCM-41-SBA-15@ACTF-ZIF-8 were fixed bed and batch adsorption. The composite of the two adsorbents gives a more favorable, economical, and affordable adsorbent to remove the heavy metals from the wastewater.

2. Experimental

2.1. Materials

All materials were purchased from (Sigma-Aldrich) product in China, and all chemicals and reagents were of analytical grade. The materials used in the present study are summarized as follows: wood powder, cationic surfactant cetyl trimethyl ammonium bromide (CTAB) (≥98% purity, tri-block copolymer Pluronic P123 [poly(ethylene glycol)-block-poly(propylene glycol)-block-poly(ethylene glycol)] molecular weight of 5,800 (>99.8% purity), tetraethyl orthosilicate (TEOS) (99.9% purity), 28% solution of ammonium hydroxide (99.9% purity), 37% hydrochloric acid (98% purity), acetic acid (>99% purity), zinc nitrate hexahydrate (99% purity), 2-methylimidazole (HMe-Im) (99% purity), absolute ethanol (98% purity), triethylamine (TEA) (99.5% purity), birchwood cellulose, isopropanol (≥95% purity), sodium hydroxide (>95% purity), sulfuric acid (>98% purity), potassium hydroxide (90% purity) and deionized water (DI).

2.2. Materials synthesis

2.2.1. MCM-41: synthesis

8 g of CTAB was dissolved in 100 mL of deionized water, which was then mixed with 100 mL of ethanol and 300 mL of 0.82 mol/L ammonia solution. The mixture was stirred vigorously for 30 min to produce a transparent solution. Under rapid stirring, 16.7 mL of TEOS was added slowly to the solution, and the pH was changed to 10, and the stirring was conducted at room temperature for 4 h. The substance was retrieved by centrifugation and washed several times with distilled water. To remove the organic surfactant template using a programmable furnace with a heating ramp of 2°C/min, the material produced was heated to 550°C for 6 h to heat the sample [36–38].

2.2.2. Synthesis of SBA-15

3.3 g of copolymer Pluronic P123 was dissolved in 102 mL water and 2 M HCl solution under stirring until full homogeneity. At 40°C, TEOS (6.93 g) was added to the solution, and the slurry was retained for 4 h under stirring. The mixture was then aged 24 h at 90°C using a polypropylene bottle for the hydrothermal method. After filtration, the obtained white powder was retrieved, washed thoroughly with deionized water, and then dried at room temperature in the open air with a heating ramp of 2°C/min [39–41]. The dried solid was calcined at 550°C for 3 h for synthesized SBA-15.

2.2.3. Synthesis of ACTF carbon nanostructure

Wood cellulose was collected as a waste product from the local market and processed using the following method: the waste material was washed vigorously with purified water to remove dust and other interference particles and washed away for a few days in sunlight. Wood powders were subjected to alkaline treatment with a 10% solution of NaOH at 100°C. The produced microcrystalline cellulose (MCC) was subsequently washed overnight with distilled water and dried at 40°C in a vacuum. The synthesis and exfoliation of the ACTF sample was performed with the catalytic acid spray method where 15 g of MCC powder was sprayed with 10% H_2SO_4 aqueous solution with spray rate 5 mL/s within 20 min [42–44]. The desired temperature was maintained at 40°C–45°C and the experiment was carried out in 5 s of pulses separated by 5 s of cooling time. The produced ACTF was calcinated and activated in a tubular furnace at 550°C for 2 h under the argon atmosphere at a heat rate of 3°C/min. To extract any unnecessary organic deposition, the resultant carbonized wood cellulose product was thoroughly washed with isopropanol. The substance was subsequently washed daily with isopropanol and deionized water to remove any impurities present in the sample. The washed specimens at 80°C have been centrifuged and dried overnight [5].

2.2.4. Synthesis of ZIF-8

0.733 g Zn $(NO_3)_2{\cdot}6H_2O$ (2.46 mmol) was dissolved in 50 mL of DI water. Another solution was prepared by stirring and dissolving 1.622 g HMe-Im (19.75 mmol) and 2.00 g TEA (19.76 mmol) in 50 mL of DI water. The Zn solution was added to the stirred HMe-Im/TEA solution, the liquid turned opaque white immediately, and the suspension was stirred for 10 min. The synthesized blend was isolated via centrifugation, the supernatant was decanted, and the solid was re-suspended in DI water. The ZIF-8 remained in the water for 12 h, and then it was removed by centrifugation and re-suspended in DI water again. The ZIF-8 suspension was centrifuged after another 12 h, and then the solid was collected and dried in the air [45,46].

2.2.5. Synthesis of quaternary nanocomposite (MCM-41-SBA-15@ACTF-ZIF-8)

During the synthesis of ZIF-8 (direct method), quaternary nanocomposite (MCM-41-SBA-15@ACTF-ZIF-8 was synthesized by incorporating MCM-41 SBA-15 and ACTF. Based on the predicted mass of the sample, MCM-41, SBA-15, and ACTF were added in 0.1 ratios. After slowly cooling to the ambient temperature, the product (MCM-41-SBA-15@ACTF-ZIF-8) nanocomposite was purified in the same way as obtaining ZIF-8.

2.3. Materials characterization

2.3.1. X-ray diffraction

The phases of different samples were investigated using two types of X-ray diffraction (XRD) instruments. The XRD patterns with a wide-angle 2θ ranging from 10° to 80° and with a 0.04°s^{-1} scanning rate were recorded by X-ray X'Pert powder diffractometer (Philips, D8-Brucker Model, Amsterdam, Netherlands). This apparatus is equipped with Ni filter and Cu Kα-radiation (λ = 1.5418 Å) at the accelerating voltage of 40 kV and applied current of 30 mA. For crystallinity and phases of ordered mesoporous silica (MCM-41 and SBA-15), another XRD instrument was used in a 2θ range from 0.5° to 10° (Bruker D8 Advance X-ray diffractometer). The samples were scanned using Bragg's configuration in 2θ range from 10° to 80° with 0.04°s^{-1} scanning rate.

2.3.2. Fourier-transform infrared spectroscopy

The Fourier-transform infrared spectroscopy (FT-IR) investigation was performed utilizing the AT1 Mattson model Genesis Series (USA) infra-red spectrophotometer. For all the samples under investigation, the KBr technique was carried out approximately in a quantitative manner since the weight of the sample and KBr were kept constant.

2.3.3. Transmission electron microscopy

The morphology of all different prepared samples was explored by a high-resolution transmission electron microscope (HRTEM), model JEM 1230 (JEOL, Japan), 120 kV, 600.000 magnifications. HRTEM instrument equipped with an energy-dispersive X-ray (EDX) facility was used to capture images and perform elemental analysis. The samples were prepared by ultrasonic dispersion, using absolute alcohol as dispersing medium for 30 min to ensure a good dispersion.

2.3.4. Scanning electron microscopy

The morphology of quaternary nanocomposite (MCM-41-SBA-15@ACTF-ZIF-8) was investigated through field-emission scanning electron microscopy (FE-SEM, Quanta FEG 250, Netherlands).

2.3.5. X-ray photoelectron spectroscopy

The crystalline structure of composite was analyzed by X-ray photoelectron spectroscopy (XPS); K-ALPHA surface examination, Thermo logical, was utilized to decide the tests' surface chemical composition and elemental chemical states.

2.4. Adsorption activity

The adsorbent quaternary nanocomposite (MCM-41-SBA-15@ACTF-ZEF-8) (20 g), an adsorption column (11 cm in height and 1.0 cm in diameter) was arranged and utilized to extract BT from the aqueous solution. At a 5.0 mL/min flow rate, roughly 200 mL of the multi-component BT arrangement (1,000 mg/L) was passed through the inactive column, and post-column divisions were collected. The results were utilized to construct the breakthrough's bend and evaluate the breaking point [47,48].

2.5. Synthetic wastewater preparation

The synthetic wastewater was prepared following an established reported protocol [6]. The pH of the synthetic wastewater was adjusted to 7.9. The initial concentration of the synthetic wastewater on an adsorption column was studied by varying the strength of the wastewater. Its chemical composition was determined to contain 5,000 mg/L of total organic carbon (TOC). An atomic absorption spectrometer, Varian FS220, was used to measure the samples' metal ion concentrations. The pH of the samples was measured with a Hach multimeter, HQD4D. Chemical oxygen demand (COD) was determined using Hach LCK314 COD vials digested in Hach DRB200 Digital Reactor and was measured using Hach DR6000 UV-Vis spectrophotometer. The TOC was determined using Hach LCK386 vials, centrifuged in Hach TOC X5 Shaker, and was measured using Hach DR6000 UV-Vis spectrophotometer with RFID technology.

2.6. Fixed-bed column experiments

The fixed-bed mode is more similar to practical produced water treatment and presents a newly developed adsorbent's beneficial adsorption properties. The prepared adsorbent was packed in the column, with a glass wool layer at both ends of the bed to ensure a good liquid distribution. The produced water solution was pumped into the bed in an upward direction using a peristaltic pump. The experiments were done at different bed heights (3.5, 5.5, and 11 mm), influent benzene and toluene concentrations (250, 500, and 1,000 mg/L), and influent flow rates (3, 6, 9 mL/min). The inlet solution's pH was set at 7.5 as an optimum value obtained in our previous study [6]. After beginning the process, the effluent sample was collected at regular time intervals, centrifuged at 3,000 rpm for 1 h, and then analyzed to obtain effluent concentration. Afterward, an accurate calibration curve was obtained. The unknown benzene and toluene solution was placed in high-performance liquid chromatography, and its results were read. Finally, its concentration was easily calculated using the calibration curve.

3. Results and discussion

3.1. Characterization of material

X-ray diffraction was one of the most important techniques for characterizing the structure of crystalline or other ordered materials. The XRD peaks do not occur from local order in the atomic spectrum, but from the ordered channel walls, in ordered porous samples MCM-41 and SBA-15. XRD measurements of small angles can typically illustrate ordered mesostructures. Diffraction X-ray patterns for the order mesoporous silica acquired at small angles are shown in Fig. 1A. The small-angle X-ray diffraction (SAXRD) pattern of MCM-41 has an extreme (100) peak feature and two

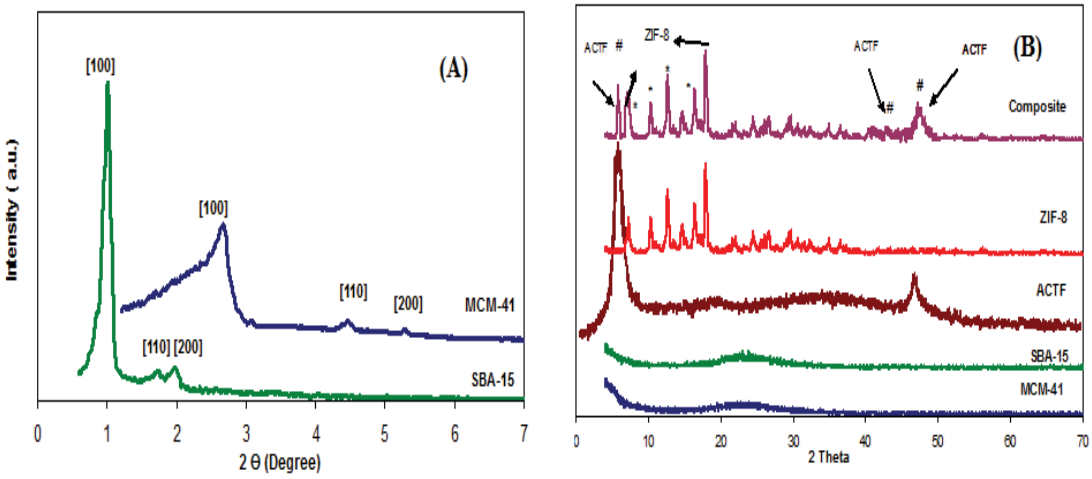

Fig. 1. SAXRD of ordered mesoporous silica (MCM-41 and SBA-15) (A) and WAXRD of ordered mesoporous silica, ACTF, ZIF-8, and quaternary nanocomposite (MCM-41-SBA-15@ACTF-ZIF-8) (B).

apparent (110) and (200) reflections at two stages, respectively 2.69, 4.5, 5.4 [49]. The strong peak (100) directly indicates the presence of MCM-41 structure, and the two weak peaks (110) and (200) can be indexed to the P6mm space group, indicating a hexagonal mesostructure material with a high degree of long-range ordering of the structure. The small-angle X-ray powder diffraction of SBA-15, three well-resolved peaks at 2θ ≈ 1.01, 1.77, and 2.01 were shown, being characteristic of planes (100), (110) and (200), representing a significant degree of long-range ordering in the structure and a well-formed 2D-hexagonal lattice [15,40,50]. Fig. 1B demonstrates patterns of prepared MCM-41, SBA-15, ACTF carbon nanostructure and quaternary nanocomposite (MCM-41-SBA-15@ACTF-ZIF-8) for a wide-angle X-ray powder diffraction (WAXRD). A broad diffusion peak or amorphous peak centered at an equivalent Bragg angle of 2θ = 23° was recorded, revealing that the main substance of the prepared silica MCM-41 and SBA-15 are amorphous phase silica. Moreover, the XRD of ACTF shown the peak at 9° was already expected for the ACTF, due to the increase in the interplanar distance between the nanoplatelets after the insertion of the oxygenated groups, as well as the peak at 26° with low intensity, referring to some remaining graphite platelets. It must be highlighted that the XRD diagram for powder ACTF was different from that presented for the ACTF, with the appearance of new peaks representing interplanar distances smaller than 0.84 nm. This can be attributed to the vacuum filtration process, which probably causes a partial restacking of graphene and graphene oxide sheets in the material. WAXRD analysis of the ZIF-8 shown sharp diffraction peaks of all the samples with 2θ values of 7.4°, 10.43°, 12.84°, 14.79°, 16.48°, 17.95°, 22.01°, 24.48°, 25.7°, 26.74°, 29.7°, 30.67° and 31.59° with crystallinity 56.8% can be well indexed to phase of ZIF-8 (JCPDS Card No. 01-072-7977) [51]. The XRD patterns of MCM-41-SBA-15@ACTF-ZIF-8 nanocomposite matching with the simulated ZIF-8 pattern and a small diffraction line is clearly detected at 9° and 26° characteristic most probably of the ACTF carbon nanostructure. This may refer to the incorporation of MCM-41, ACTF and ZIF-8 into SBA-15 framework, in some highly dispersed state. Moreover, incorporation of MCM-41 and ACTF seems to locate on the top surface of the ZIF-8 matrix which was consistent with the scanning electron microscopy (SEM) results.

The FT-IR spectra of mesoporous silica MCM-41, SBA-15, ACTF, ZIF-8, and quaternary nanocomposite (MCM-41-SBA-15@ACTF-ZIF-8) are shown in Fig. 2. The spectra of MCM-41 show similar vibrational bands characteristic of silica (SiO_2). At 3,460 cm^{-1}, the wideband was due to the stretching vibration of H_2O molecules. The IR band at 1,650 cm^{-1} was correspondingly due to the bending vibration of H_2O molecules. The shoulder at 3,250 cm^{-1} in SiO_2 structure may be attributed to the stretching vibrations of Si–OH groups. Typically, the Si–O–Si asymmetric stretching vibrations were assigned to the very powerful and wide IR band at 1,110 cm^{-1}, with a shoulder at 1,230 cm^{-1}. IR band at 983 cm^{-1} was attributed to the Si–OH bending (silanol groups). SiO–H symmetrical stretching vibrations can be assigned to the IR band at 815 cm^{-1}, while the IR band at 470 cm^{-1} can be attributed to the O–Si–O bending vibrations [52,53]. FT-IR spectra of ACTF prepared showed the presence of oxygen-containing functional groups in ACTF. The peak at 3,412 cm^{-1} indicates the stretching of a hydroxyl group, C=O carbonyl stretching at 1,723 cm^{-1}, and the C–O epoxide group stretching at 1,178 and 1,073 cm^{-1}. The high intensity of major peaks in ACTF reveals that a large amount of oxygen-containing groups were present after the oxidation process. The peak at 1,620 cm^{-1} was related to the skeletal stretching of the C=C alkene group. For ZIF-8, there was the presence of triethylamine indicated by the TEA C–N stretch at 1,210 cm^{-1}, which was the strongest adsorbing peak in the TEA spectrum. The adsorptions from 3,200 to 2,700 cm^{-1} were indicative of both protonated HMe-Im and TEA. The N–H stretching band was visible at 3,135 cm^{-1} and the C–H stretching bands of the methyl groups at 2,929 (imidazole

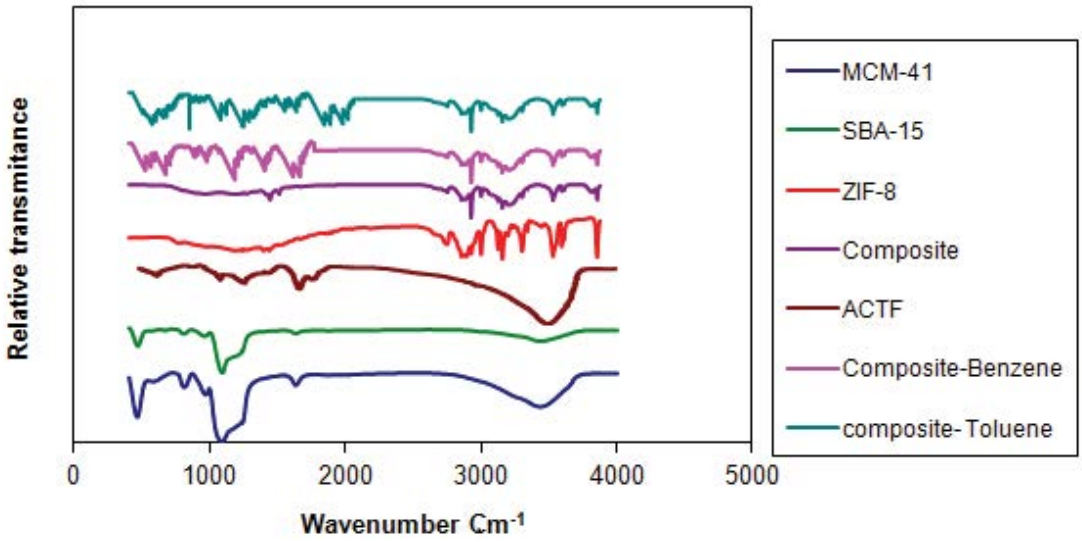

Fig. 2. FT-IR of ordered mesoporous silica of MCM-41, SBA-15, ACTF, ZIF-8, nanocomposite (MCM-41-SBA-15@ACTF-ZIF-8), nanocomposite after benzene sorption, and nanocomposite after toluene sorption.

aliphatic C–H) and 1,307 cm^{-1}. The band corresponding to C–N and C=N was located at 1,457, 1,423 and 1,145 cm^{-1}.

The absorption band at 450 cm^{-1} was related to Zn–N stretching, and the arrangement of the bands was in agreement with that expected for the organic ligand, and similar results are reported in the literature [52]. It was observed that the spectra of the samples are in good agreement with other studies. For quaternary nanocomposite (MCM-41-SBA-15@ACTF-ZIF-8) showed no remarkable differences were observed compared with ZIF-8 except two peaks at 1,230 cm^{-1} for the characteristic peak of Si–O–Si asymmetric stretching vibrations of mesoporous silica SiO_2 (MCM-41 and SBA-15) and another peak at 1,178 cm^{-1} is usually assigned to C–O epoxide group stretching of ACTF. The FT-IR spectrum of the composite after benzene and toluene sorption data was observed at broad peaks between 1,633 and 1,548 cm^{-1} for toluene adsorbed and 1,401, 1,339 cm^{-1} for benzene were related to aromatic rings. Also, peaks 1,658 and 1,831 cm^{-1} for toluene and benzene were associated with the aromatic ring stretching of C=C bonds, and peaks at about 1,221 cm^{-1} (benzene), 1,202 cm^{-1} (toluene) that related to C–H bonds of the aromatic ring were observed.

Moreover, broad peaks between 3,296 and 3,525 cm^{-1} for toluene and 3,301, 3,525 cm^{-1} for benzene were observed. Due to hydroxyl functional groups from benzene sorption, the broad peak between 1,400–1,450 cm^{-1} was observed. Daifullah and Girgis [54] investigated the adsorption of benzene, toluene, ethylbenzene, and p-xylene on activated carbons that contained surface groups similar to those found on the composite of ACTF synthesized from various precursors. They reported that both textural properties and surface chemistry influence uptake of the aromatics. At a solution pH of 7, the prepared composite with higher surface acidity had a higher benzene adsorption capacity. This was attributed to the increase in dispersive interaction with increasing carbon basicity. The interaction of the π orbital electrons in the carbon basal plane with the aromatic rings of benzene and toluene was favored. The benzene and toluene maximum adsorption capacity of the adsorbent composite compared to the various adsorbents reported in the literature was far higher. It could be attributed to the better porous nature as well as its surface chemistry. A benzene and toluene adsorption capacity of near 1,000 mg/L has not been reported in the open literature, which promises porous prepared composite to be a potential adsorbent for feasible commercial applications.

The structural of MCM-41, SBA-15, ACTF, ZIF-8, and quaternary nanocomposite (MCM-41-SBA-15@ACTF-ZIF-8) samples can be directly observed by transmission electron microscopy (TEM) are shown in Fig. 3. TEM images of the mesoporous silica MCM-41 as shown in Fig. 3A, demonstrate the well-ordered hexagonal arrays of mesopores presented along the path of the channel. In the case of SBA-15 shown in Fig. 3B, there were sets of hexagonally well-ordered mesoporous channels running along the length of the particles, and it is clear that the wall thickness of SBA-15 (2.88 nm) was increased. This confirms the successful intense homogenous layer in the channels of the ordered mesoporous SBA-15, and the TEM image of ACTF shown in Fig. 3C illustrates the dark areas and indicates the thick stacking nanostructure of several ACTF and/or graphene layers with some amount of oxygen functional groups. The higher transparency areas indicate much thinner films of a few layers of ACTF oxide resulting from stacking nanostructure exfoliation. A significantly larger surface area of the high transparency of delaminated graphene layers (of about one too few-layer thickness) was shown by the ACTF sample, indicating layer elimination due to reduction.

Moreover, the morphology of ZIF-8 and its composites was studied using TEM, as shown in Fig. 3D, which illustrates well-shaped rhombic dodecahedron crystals, showing good agreement with the literature [55] where sizes of ZIF-8 crystals were between 46 to 60 nm. The morphology of quaternary nanocomposite (MCM-41-SBA-15@ACTF-ZIF-8) shown in Fig. 3E illustrates the nucleation of ZIF-8 inside the pores of SBA-15 was more favorable than outside of SBA-15. Thus, the ZIF-8 crystal growths were formed inside the pores of SBA-15 rather than outside due to the direct in situ synthesis of ZIF-8. Moreover, rhombic dodecahedron crystals structure of ZIF-8 dispersed on the surface of SBA-15 and incorporated of ACTF, and MCM-41 with SBA-15 appears as a dark sheet.

EDX scan and elemental mapping are shown in Fig. 4 of quaternary nanocomposite (MCM-41-SBA-15@ACTF-ZIF-8); the EDX scans of region exhibit the Si and O (owing to MCM-41 and SBA-15) as well as C peaks increase in the carbon content were observed in the EDX scan of the region this observation due to the TEM grid, ACTF, and ZIF-8 further confirm that ZIF-8, ACTF, and MCM-41 occupied the pores of SBA-15. On the other hand, Zn and N peaks were observed in the EDX scan of the region. This observation further confirms that ZIF-8 occupied the pores of SBA-15 on the surface of ZIF-8.

The SEM images of the MCM-41-SBA-15@ACTF-ZIF-8 nanocomposite sample are shown in Fig. 5A. The quaternary superposition prepared in the research is a unique combination of several silicon shapes with carbon nanostructures such as ACTF, leading to many surface shapes with multiple surface areas and different functional groups in chemical composition susceptibility different BTEX. The quaternary superposition's expected shape can be visualized as a large block of SBA-15 in cylindrical tubes with microporous holes on their surface and mesoporous holes in the main openings of these tube cylinders.

Inside this mold and on a surface, it enters both MCM-14 and ACTF and ZEF-8 in multiple images where the ACTF appears in the form of slides interfering in the SBA-15 wall in the exterior surface only, which indicates that a lot of the carbon shape inside the SBA structure is not merging. In quaternary composite, we can see the scattering of the ZIF-8 on the surface of the silica mold as large cubes in the range of 50 nm. As for the MCM-4, we can see that the form of pellets or nanoparticles in the range of 20–30 nano and condensed inside the wire cylinders of the SBA-15. Fig. 5B over the quaternary composite's synthesis showed the superposition's vacuum position. We notice many gaps inside the prepared superposition, which have a high electron density and variety. This gives the impression of a high surface area that allows adsorption to a high degree of BTEX [56–58]. Carbon needles from the edges of the ACTF appearing in a stereotype with folds in shape as a result of competition and streak hindrances of the functional groups present in the quaternary composite give a form that helps in the process of catalysis

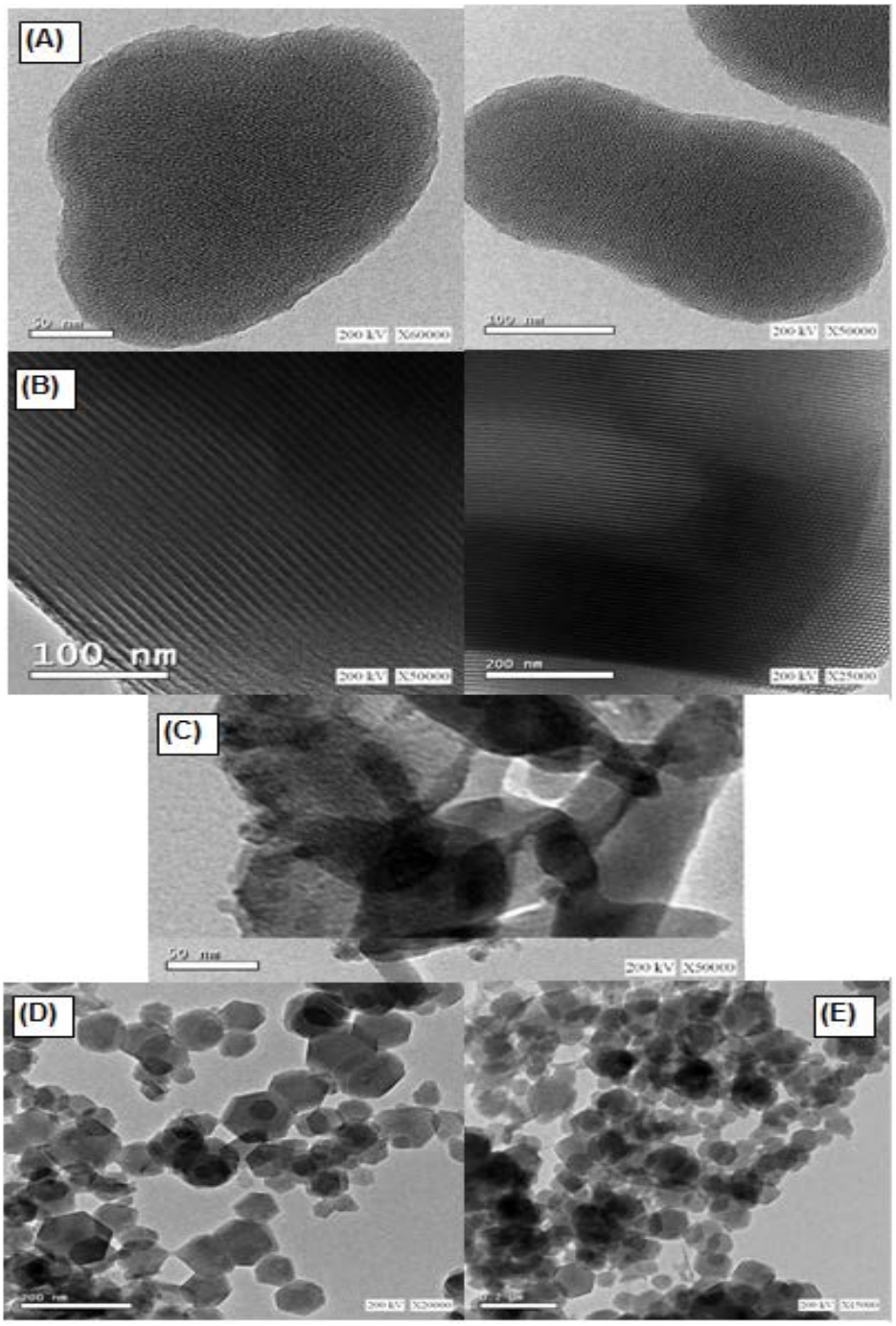

Fig. 3. TEM images of samples: MCM-41 (A), SBA-15 (B), ACTF (C), ZIF-8 (D) and MCM-41-SBA-15@ACTF-ZIF-8 (E).

and chemical cracking in addition to adsorption as used in this research.

XPS results: The surface composition and chemical states can be determined using the XPS spectrum according to the characterizing binding energies of the different elements on material surfaces. Fig. 6a shows a survey XPS spectrum of MCM-41-SBA-15@ACTF-ZIF-8 composite indicate the presence of the following elements: Si, Zn, O, C, and N surface with small contaminates of Cl. Fig. 6b suggests that the binding energy spectrum of Si2p was 102.5 eV belong to Si–O bonds. This demonstrates that Si elements migrate to the composite surface to form Si–O–Si structure. Fig. 6c, the high-resolution Zn2p spectrum exhibited two strong peaks at 1,044 and 1,021 eV, which are well assigned to the $Zn2p^{1/2}$ and $Zn2p^{3/2}$, respectively. It indicated that Zn in the composite. The 13 eV difference between $Zn2p^{3/2}$ and $Zn2p^{1/2}$ indicates the oxidation state +2 for Zn ions in composite, which may reveal the presence of ZIF-8. The C1s XPS spectra of MCM-41-SBA-15@ACTF-ZIF-8 composite shown in Fig. 6d have two peaks

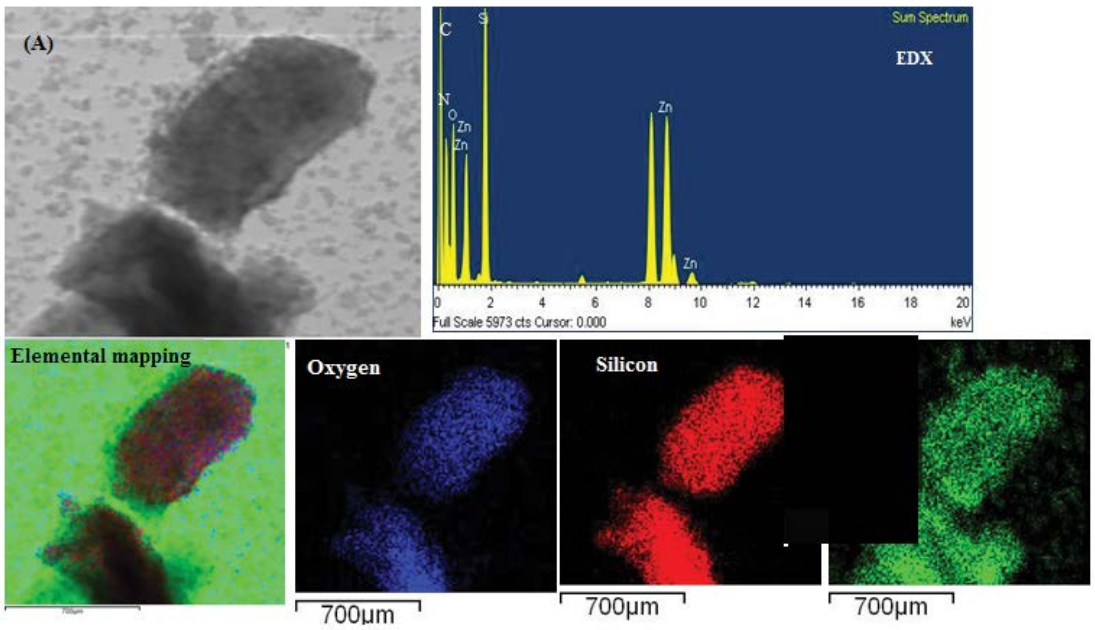

Fig. 4. EDX scans and elemental mappings of MCM-41-SBA-15@ACTF-ZIF-8 composite.

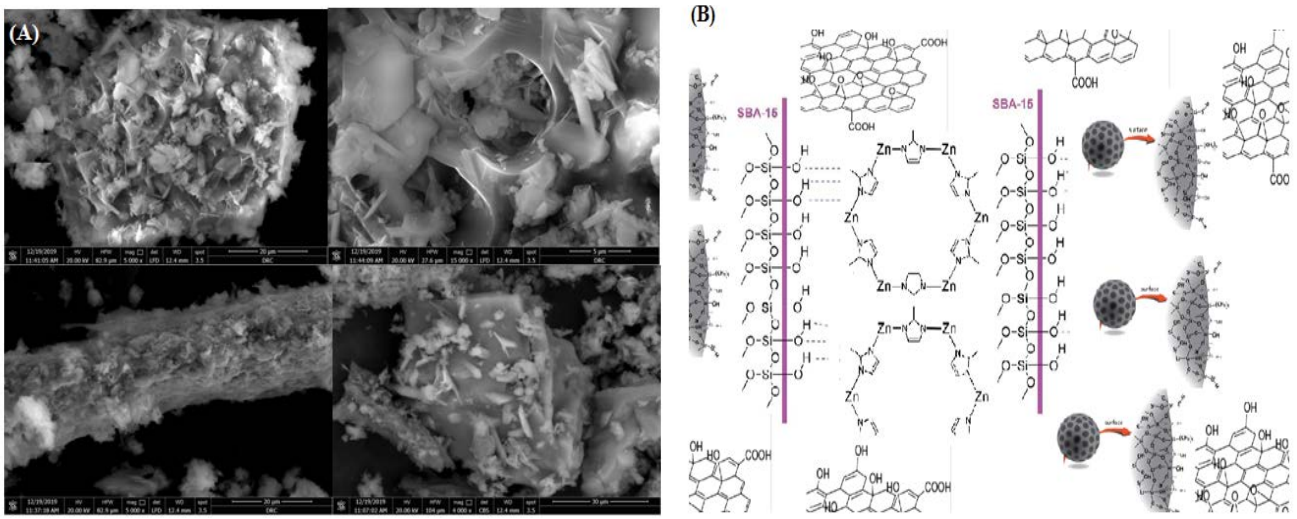

Fig. 5. SEM of MCM-41-SBA-15@ACTF-ZIF-8 nanocomposite (A) and the overall synthesis of MCM-41-SBA-15@ACTF-ZIF-8 nanocomposite (B).

at 284.92 eV corresponds to the C–N band from imidazole, and another peak at 291.09 eV was related to the presence of carbonates C–C, C–H, and C–OH. The O1s spectrum signal for composite consisted of three peaks associated with the O–C carbonate, Zn–OH, and O–Si–C, respectively, characterized by binding energies around 530.59, 534.59, and 535.8 eV shown in Fig. 6e. The high-resolution of XPS of N shown in Fig. 6f, which can be two peaks. These two peaks with binding energy at 399.09 and 398.51 eV corresponding to imidazole and pyridinic, respectively, related to Zn–Im2 defects on the external surface of the nanostructured ZIF-8 with decreasing particle size.

3.2. Column activity results

3.2.1. Breakthrough curves

The breakthrough curves were obtained by plotting C/C_0 vs. the 10 mg/L BT solution volume to assess both the saturation volume and power. The breakthrough curves for the BT examination are shown in Fig. 7. Fig. 7 indicates that the breakthrough volumes are 35 mL, and the saturation volumes (V_x) at 50 min (t_x) were found to be 80 mL. The maximum BT removal capacity within the column is determined. The Q value was 700 mg/g. Parameters of the operational column are accommodating within the design of a fixed adsorbent to remove BT from a watery solution [48,59].

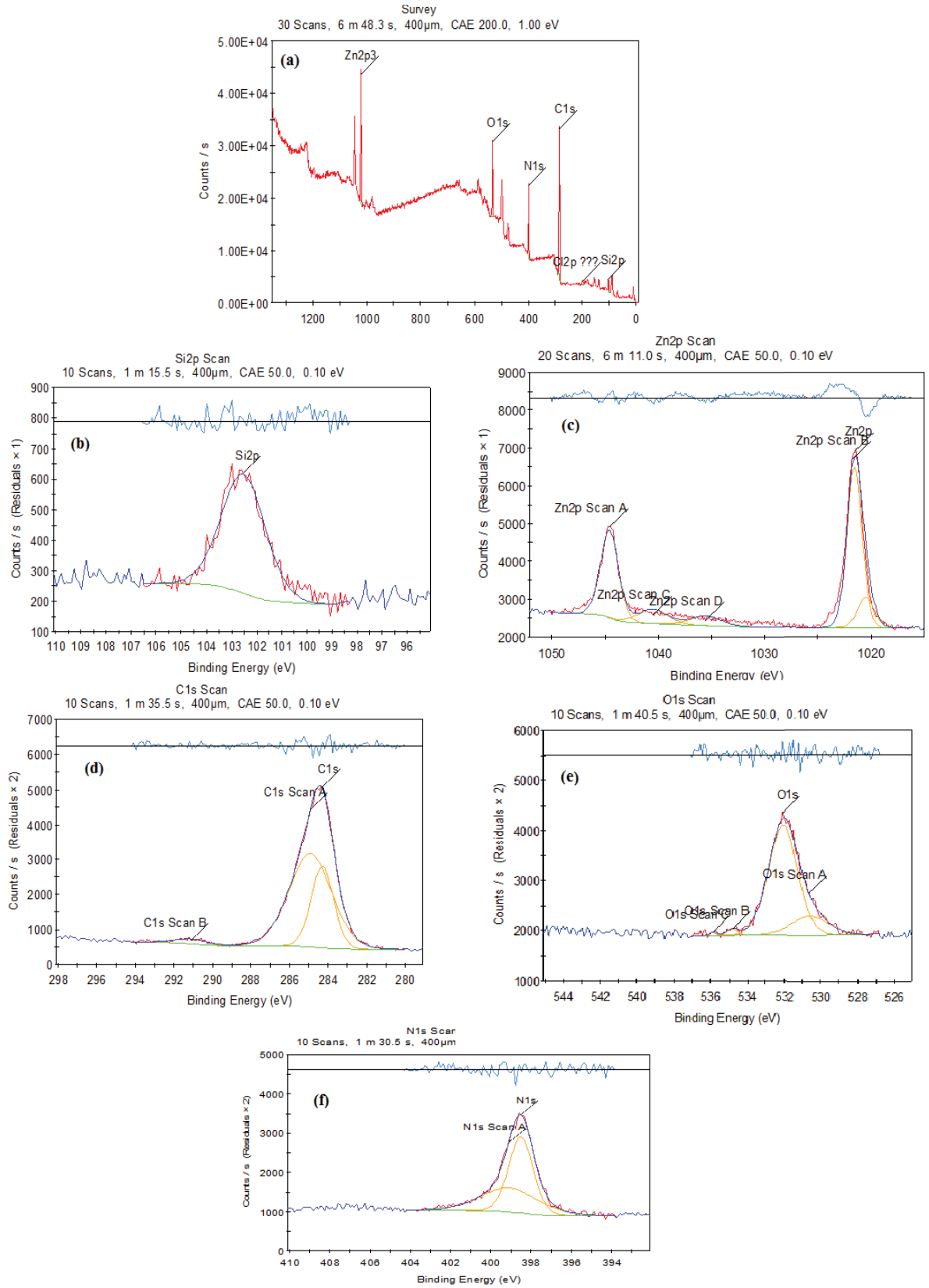

Fig. 6. XPS results of MCM-41-SBA-15@ACTF-ZIF-8 composite, (a) survey spectrum of composite, (b) high-resolution spectra of Si2p, (c) high-resolution spectra of Zn2p (binding energy (d) high-resolution spectra of C1s, (e) high-resolution spectra of O1s and (f) high-resolution spectra of N1s.

3.2.2. Bed height effect

Breakthrough curves were accomplished from BT adsorption on prepared quaternary nanocomposite (MCM-41-SBA-15@ACTF-ZIF-8) at diverse bed heights (11, 5.5, and 3.5 cm) with a starting BT concentration of 1000 mg/L of BT and a flow rate of 5 mL/min, as depicted in Fig. 8.

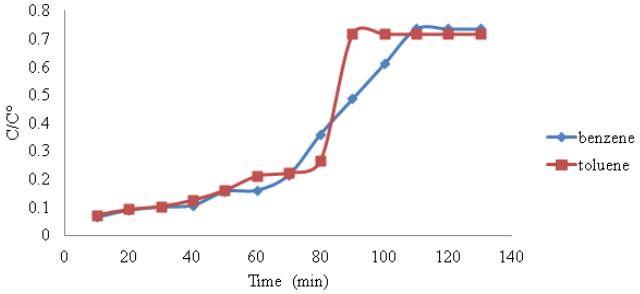

Fig. 7. Breakthrough curves for benzene (A), toluene (B), BT concentration: 1,000 mg/L; flow rate: 5 mL/min; bed height: 11 cm; room temperature: 28°C ± 2°C.

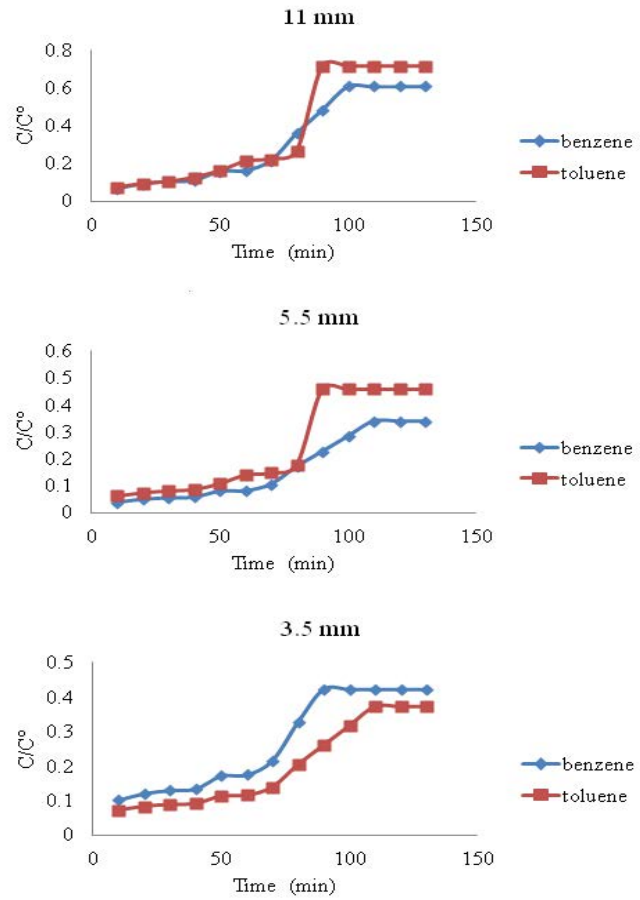

Fig. 8. Breakthrough curves for adsorption of BT on quaternary nanocomposite (MCM-41-SBA-15@ACTF-ZIF-8) beds at different heights (C_0 = 1,000 mg/L; Q = 5 mL/min).

As the bed height increased from 3.5 to 11 cm, the rate of BT removal decreased from 40% to 54.57%, which agrees with references [49,60]. It was noted that the time to realize the breakthrough decreased due to bed height was more upright than 3.5 and 5 cm bed heights. When the height of the bed was reduced, the adsorbent load within the column decreased that due to the reduction take place in the available active site on the present composite in the column during the adsorption process, and the rate of adsorption increased more quickly.

Over time, the sorbent substance was saturated, and subsequently, the BT concentration increased within the effluent solution. Several active sites linked to the BT were progressed by increasing the height of the bed by expanding the absorbent surface area. By increasing the height of the bed, the conveyance of the contaminant and the capacity of the sorbent material increased the removal of BT, in this way dealing with more amounts and volumes of wastewater and improving the removal quality. This observation indicates slower transport due to decreased diffusion coefficient or mass transfer coefficient, as shown in Fig. 8 [9]. This explanation was supported by other investigators [61].

3.2.3. Flow rate effect

The impact of the flow rate of 3–9 mL/min on the breakthrough of benzene and toluene at a bed height of 11 cm and initial beginning benzene concentration of 1,000 mg/L is shown in Fig. 9. It can be found that as the breakthrough curves approach the origin, the saturation times and breakthrough focuses for benzene and toluene diminish at high flow rates. The increase in flow rate (i.e., diminish in residence time) leads to a reduction in the thickness of the surface film, which, in impact, is considered as resistant to mass transfer and consequently increases the rate of mass transfer [47]. At feed flow levels of 1.0 and 2.7 mL/min, benzene hits breakthrough concentrations (C_e/C_0 = 0.1) at a time of 15 and 5 min, respectively. With increased flow rate, the adsorbate effluent to noticeable concentration proportion increments more quickly. The C_e/C_0 values are 0.539 and 0.754 for toluene at a time of 30 min, respectively, at flow rates of 3 and 6 mL/min. Toluene is more unequivocally adsorbed than benzene; thus, it uproots the adsorbent and shows up within the effluent stream at an early stage with a higher concentration than was initially displayed within the originally presented in the feed, as appeared clearly in Fig. 9 at a 3 mL/min flow rate. This activity was known as the marvel of overshoot or rolled up that is carried out due to the competitive adsorption of the exceedingly adsorbed compound (toluene) and was hence displaced by more of the weakly adsorbed compound (benzene). The brief breakthrough time of benzene and its displacement by toluene is attributed to both the moderate adsorption of benzene on the adsorbent surface and its high volatility [62]. This action for the considered strategy affirms the accomplishment of 395, 270, and 150 min benzene saturation (C_e/C_0 = 1) comparing to feed flow rates of 3–9 mL/min, respectively. On the other hand, toluene requires more time and a high flow rate to reach saturation where a most extreme C_e/C_0 of 0.887 and a flow rate of 3 mL/min have been accomplished at the time of

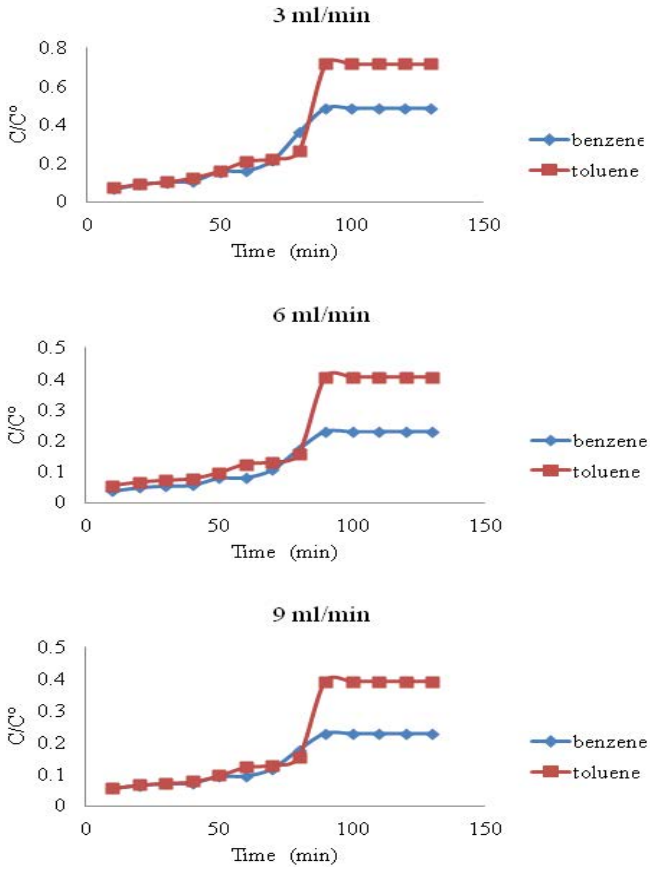

Fig. 9. Effect of flow rate on the breakthrough of benzene and toluene at a bed height of 11 cm and initial benzene concentration of 0.1 g/mL on quaternary nanocomposite (MCM-41-SBA-15@ACTF-ZIF-8).

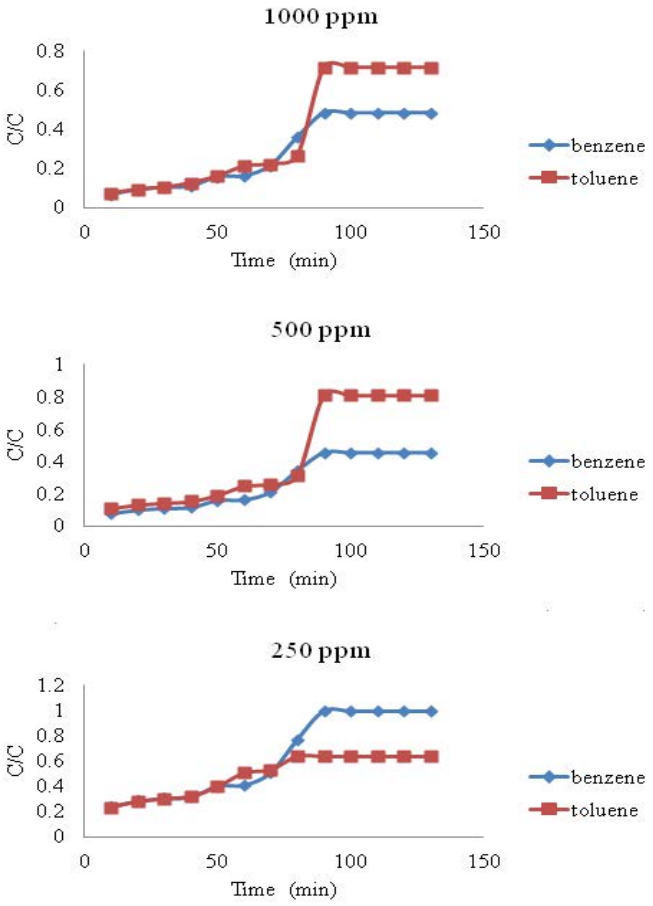

Fig. 10. Benzene conc. effect in the range of 250–1,000 mg/L on quaternary nanocomposite (MCM-41-SBA-15@ACTF-ZIF-8).

90 min. Similar perceptions for fixed-bed adsorption of toluene on ZSM-5/fiber composite [52] were recorded by [51,53].

3.2.4. Effect of initial concentrations

The initial concentration effect of 250–1,000 mg/L benzene on quaternary nanocomposite (MCM-41-SBA-15@ACTF-ZIF-8) breakthrough benzene and toluene curves is examined at a consistent flow rate of 3 mL/min and 11 cm in bed height (Fig. 10). It can be observed that a diminish in breakthrough time, and steepness in breakthrough curves was caused by a rise in the inlet concentration of benzene. This may be due to an enhancement in the driving force of mass transfer through the liquid film. On the side, an increment in the rate of adsorption results in quick adsorbent saturation [20,52]. The C_e/C_0 values were 0.496 and 0.819, respectively, for the initial benzene concentration of 250–1,000 mg/L at time of 80 min. The C_e/C_0 values were 0.8759 and 0.98, respectively, for initial toluene concentrations of 250 and 500 mg/L at the same time. Appropriately, a decrease in the saturation time of benzene from 90 to 70 min was observed when its initial concentration was increased from 250 to 500 mg/L.

Moreover, for toluene at 90 min and 1,000 mg/L initial concentrations, saturation was achieved (Fig. 10). The same conclusion was drawn by [42,55] investigating the competitive adsorption of benzene and toluene on macro-reticular gums from aqueous solutions. Therefore, the high driving force due to the high benzene and toluene concentration led to better column performance. Also, it was observed that the adsorption capacity was not proportionally increased with increasing influent concentration. As a result, the adsorption capacity of benzene and toluene was higher when the inlet concentration increased [9].

3.3. Adsorption modeling

With a validated mathematical model, fixed-bed adsorption results are approved to anticipate breakthrough curves and pick model parameters. Utilizing Bohart–Adams, Thomas, and Yoon–Nelson motor models, the breakthrough curves used experimental information within the range (0.01 < values < 0.99). The Thomas model assesses the adsorbent in the general solid-phase concentration of solute and the fixed-bed rate consistent, which assumes insignificant axial and radial scattering within the fixed bed; adsorption following the adsorption-desorption isotherm of Langmuir; and driving drive rate following the second-order reversible kinetic reaction (refer to the supplementary file for model equations) [63,64]. Table 1 summarizes the model parameters. All three kinetic models (Bohart–Adams, Thomas, and Yoon–Nelson) better define BTEX's simultaneous fixed-bed

Table 1
Characterization of Thomson model, Bohart–Adams, and Yoon–Nelson models values

Yoon–Nelson					
Bed height	BTEX	k_{YN}	τ	R^2	
11 mm	Benzene	0.0046266	–8.1726237	0.897685	
	Toluene	0.007880847	–11.691939	0.789528	
5.5 mm	Benzene	0.0046266	–3.9621371	0.897685	
	Toluene	0.007697401	–7.2268374	0.775897	
3.5 mm	Benzene	0.0046266	6.61128209	0.897685	
	Toluene	0.007697401	–6.0352263	0.775897	
Thomson model					
Bed height	BTEX	k_{TH}	Q_m	R^2	
11 mm	Benzene	4.04158E-06	–10709836	0.897685	
	Toluene	4.98598E-06	–29209930	0.789528	
5.5 mm	Benzene	4.04158E-06	–5192192.7	0.897685	
	Toluene	4.86992E-06	–18054781	0.775897	
3.5 mm	Benzene	4.04158E-06	8663771.56	0.897685	
	Toluene	4.86992E-06	–15077784	0.775897	
Bohart–Adams model					
Bed height	BTEX	U_0 (cm/min)	k_{AB} (L/mmol min)	N_0 (mmol/L)	R^2
11 mm	Benzene	0.3	0.001606634	22.62435976	0.97567
	Toluene	0.3	0.001401256	33.27067287	0.94928
5.5 mm	Benzene	0.3	0.001429874	30.46056151	0.97038
	Toluene	0.3	0.001193868	46.25128252	0.92379
3.5 mm	Benzene	0.3	0.001135019	49.35148185	0.9594
	Toluene	0.3	0.001157212	49.35148185	0.92063

adsorption from an aqueous system based on high values than 0.85 and low values than 0.99.

3.4. Models fitting

The Yoon–Nelson model can be respected here as a rearranged form of the models of Bohart–Adams and Thomas. The breakthrough curves were congruous from a mathematical point of view. All error functions were indistinguishable when the curve fitting was carried out for the Bohart–Adams, Thomas, and Yoon–Nelson models. The k_{YN} and ß parameters can be regarded as lumped parameters combining such operating characteristics. In other words, in a continuous column adsorption system, the magnitude of k_{YN} and τ was dependent on the initial operating conditions. The above relationships also showed that the physical significance of the words q_{om}/vc_o and a_{ox}/uc_o could reflect the operating time needed to achieve a breakthrough of 50% and that k_{YN} was numerically equal to k_{BA} (kT) and c_o. Due to the implementation of an additional adjustable h parameter, it was predicted that the three fractal-like breakthrough models should have better fitting results. The fractal-like Bohart–Adams and fractal-like Thomas models had the same mathematical shapes, subsequently coordinating their breakthrough curves and error functions. The initial pattern of the breakthrough curve follows the model of Bohart–Adams. In this scenario, an adjustment of up to 50% of the initial concentration was made. The show utilized was satisfactory, with an average R^2 of approximately 0.98.

A strong fitting with the Bohart–Adams model indicated that the rate-limiting stage within the adsorption process was surface diffusion [65]. Even though the model gives a clear and detailed approach to adsorption-column tests running and assessing, its integrity is constrained to various conditions used [65]. Thomas model showed the most higher normal of R^2, nearly 0.9629, among the three models tested. In any case, comparing the q_{TH} parameter with the test benzene and toluene adsorption capacity (q_{exp}) appeared a lower normal error than the comparison of the Yan model with the q_Y parameter. Generally, for the Yan model, the determination coefficients (R^2) that appeared in Fig. 11 were less prominent. Due to its roughly curved form close to the saturation region, the Yan model gives a poor-fitting fit of the breakthrough curve compared to the Thomas model. Agreeing with the authors, by limiting the mathematical errors of the of the Yan, the Thomas model improves the adaptation of experimental data [66]. Thomas model adopts a Langmuir-type adsorption–desorption, isothermal, and isobaric operating conditions in Fig. 12, a constant column void fraction, no radial and/or axial dispersion second-order reversible kinetics [67]. Thomas model was able to resolve the disadvantage, and both had the same concerns [68]. BTEX adsorption on quaternary nanocomposite (MCM-41-SBA-15@ACTF-ZIF-8) followed

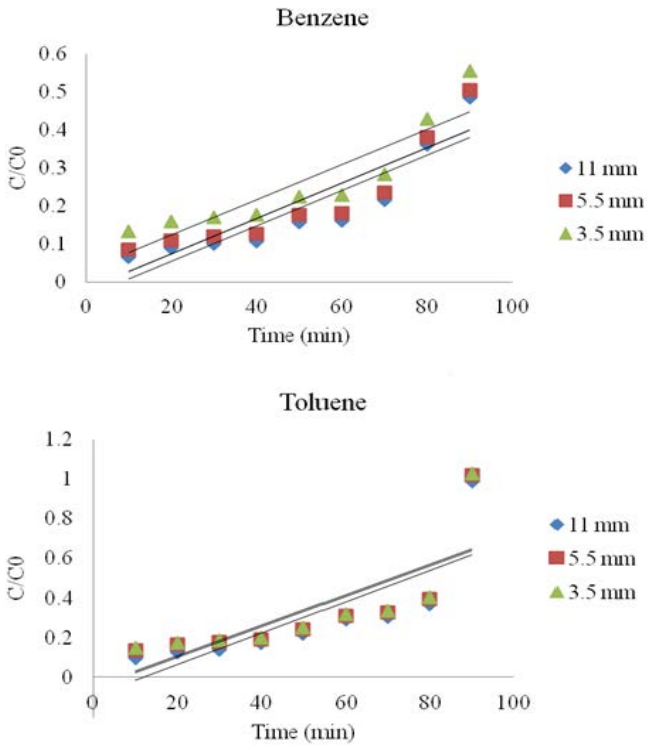

Fig. 11. Linearized Yoon–Nelson model plot at 50% breakthrough for adsorption of 1,000 mg/L of BT solution with 3 mL/min flow rate at different bed depths: 11, 5.5 and 3.5 mm on quaternary nanocomposite (MCM-41-SBA-15@ACTF-ZIF-8).

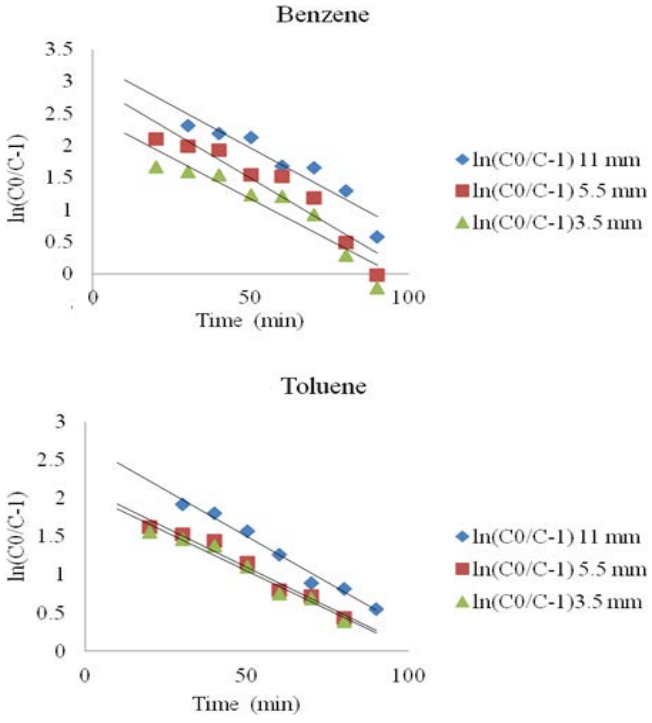

Fig. 12. Linearized Thomas model plot at 50% breakthrough for adsorption of 1,000 mg/L BT solution with 3 mL/min flow rate at different bed depths: 11, 5.5 and 3.5 mm on quaternary nanocomposite (MCM-41-SBA-15@ACTF-ZIF-8).

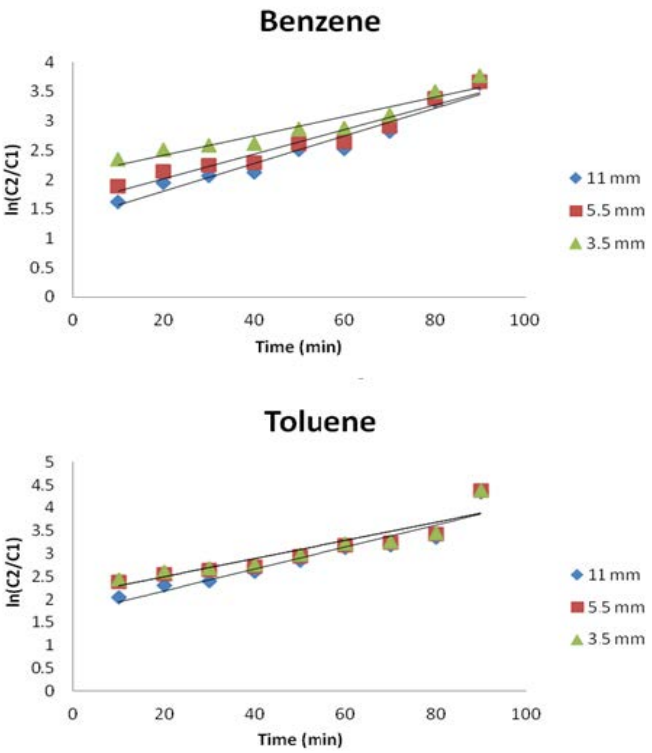

Fig. 13. Bed depth service time plot at 50% breakthrough in a fixed-bed column at different bed highest (C_0 = 1,000 mg/L).

the pseudo-second-order equation more closely than the pseudo-first-order model. In expansion, the equilibrium adsorption compared to Freundlich was better characterized by the Langmuir model. These two findings were contemplations of the Yan and Thomas models that can relate batch adsorption to the behavior of the fixed-bed column that appeared in Fig. 13. As a result of the high adsorbate–adsorbent affinity and a large number of available binding sites, BTEX quaternary nanocomposite adsorption (MCM-41-SBA-15@ACTF-ZIF-8) has been revealed to be a robust positive start-up process due to high adsorbate–adsorbent affinity and a large number of binding sites which are accessible. The equilibrium is attained once these binding sites have been completed in agreement with the Langmuir assumption of monolayer adsorption as given in many previous studies [10,11,68,69].

4. Conclusions

- Preparation of quaternary nanocomposite (MCM-41-SBA-15@ACTF-ZIF-8) was conducted via incorporation of ordered mesoporous silica MCM-41, SBA-15, and thin-film carbon nanostructure (ACTF) by one-pot synthesis during synthesis of MOF (ZIF-8).
- The study of a fixed bed and batch adsorption on quaternary nanocomposite synthesis (MCM-41-SBA-15@ACTF-ZIF-8) was conducted using benzene and toluene (aromatic hydrocarbons).
- The quaternary nanocomposite (MCM-41-SBA-15@ACTF-ZIF-8) was ideal for small-size aromatic ring selective adsorption, and its interaction was mainly influenced

by the interactions of electrostatic and π-π stacking.
- The batch adsorption study showed that toluene was more adsorbed than benzene on quaternary nanocomposites. The high competition of toluene over benzene was verified in analyzing the governing variables that affect the breakthrough curve for both adsorbates on the composite.
- The adsorption kinetics of benzene and toluene reached equilibrium at 120 min, and the pseudo-second-order kinetics model was the most suitable for experimental data, and adsorption rate constants were 0.494 and 0.413 g/g min for benzene and toluene, respectively

References

[1] R. Hosny, M. Fathy, M. Ramzi, Th. Abdel Moghny, S.E.M. Desouky, S.A. Shama, Treatment of the oily produced water (OPW) using coagulant mixtures, Egypt. J. Pet., 25 (2016) 391–396.

[2] A. Fakhru'l-Razi, A. Pendashteh, L.C. Abdullah, D.R.A. Biak, S.S. Madaeni, Z.Z. Abidin, Review of technologies for oil and gas produced water treatment, J. Hazard. Mater., 170 (2009) 530–551.

[3] A.R. Bielefeldt, H.D. Stensel, Evaluation of biodegradation kinetic testing methods and longterm variability in biokinetics for BTEX metabolism, Water Res., 33 (1999) 733–740.

[4] C.T. Scurtu, Treatment of Produced Water: Targeting Dissolved Compounds to Meet a Zero Harmful Discharge in Oil and Gas Production, Thesis for the degree of Philosophiae Doctor, Norwegian University of Science and Technology, Trondheim, June 2009.

[5] M. Aivalioti, I. Vamvasakis, E. Gidarakos, BTEX and MTBE adsorption onto raw and thermally modified diatomite, J. Hazard. Mater., 178 (2010) 136–143.

[6] L. Mohammadi, E. Bazrafshan, M. Noroozifar, A. Ansari-Moghaddam, F. Barahuie, D. Balarak, Adsorptive removal of benzene and toluene from aqueous environments by cupric oxide nanoparticles: kinetics and isotherm studies, J. Chem., 2017 (2017) 2069519, doi: 10.1155/2017/2069519.

[7] M. Fazlzadeh Davil, R. Rostami, A. Zarei, M. Feizizadeh, M. Mahdavi, A.A. Mohammadi, D. Eskandari, A survey of 24 hour variations of BTEX concentration in the ambient air of Tehran, J. Babol Univ. Med. Sci., 14 (2012) 50–55.

[8] M. Aivalioti, D. Pothoulaki, P. Papoulias, E. Gidarakos, Removal of BTEX, MTBE and TAME from aqueous solutions by adsorption onto raw and thermally treated lignite, J. Hazard. Mater., 207–208 (2012) 136–146.

[9] A.K. Mathur, C.B. Majumder, S. Chatterjee, Combined removal of BTEX in air stream by using mixture of sugar cane bagasse, compost and GAC as biofilter media, J. Hazard. Mater., 148 (2007) 64–74.

[10] B. Bina, H. Pourzamani, A. Rashidi, M.M. Amin, Ethylbenzene removal by carbon nanotubes from aqueous solution, J. Environ. Public Health., 2012 (2012) 817187, doi: 10.1155/2012/817187.

[11] J.S. Beck, J.C. Vartuli, W.J. Roth, M.E. Leonowicz, C.T. Kresge, K.D. Schmitt, C.T.W. Chu, D.H. Olson, E.W. Sheppard, S.B. McCullen, J.B. Higgins, J.L. Schlenker, A new family of mesoporous molecular sieves prepared with liquid crystal templates, J. Am. Chem. Soc., 114 (1992) 10834–10843.

[12] S. Huh, J.W. Wiench, J.-C. Yoo, M. Pruski, V.S.-Y. Lin, Organic functionalization and morphology control of mesoporous silicas via a co-condensation synthesis method, Chem. Mater., 15 (2003) 4247–4256.

[13] R.E. Morsi, R.S. Mohamed, Nanostructured mesoporous silica: influence of the preparation conditions on the physical-surface properties for efficient organic dye uptake, R. Soc. Open Sci. 5 (2021) 172021, doi: 10.1098/rsos.172021.

[14] M. Kruk, M. Jaroniec, C.H. Ko, R. Ryoo, Characterization of the porous structure of SBA-15, Chem. Mater., 12 (2000) 1961–1968.

[15] R. Huirache-Acuña, R. Nava, C.L. Peza-Ledesma, J. Lara-Romero, G. Alonso-Núñez, B. Pawelec, E.M. Rivera-Muñoz, SBA-15 mesoporous silica as catalytic support for hydrodesulfurization catalysts — review, Materials (Basel), 6 (2013) 4139–4167.

[16] L.T. Gibson, Mesosilica materials and organic pollutant adsorption: part A removal from air, Chem. Soc. Rev., 43 (2014) 5163–5172.

[17] H.H. El-Maghrabi, R. Hosny, M. Ramzi, M.M. Abdou, M. Fathy, Novel mesoporous silica (MCM-41) and its characterization for oil adsorption from produced water injected in water injection projects using fixed-bed column processes, Desal. Water Treat., 60 (2017) 70–77.

[18] H. Vinh-Thang, Q. Huang, M. Eić, D. Trong-On, S. Kaliaguine, Adsorption of C_2 hydrocarbons on biporous SBA-15 mesoporous silica, Langmuir, 21 (2005) 5094–5101.

[19] E.C. Santos, L.S. Costa, E.S. Oliveira, R.A. Bessa, A.D.L. Freitas, C.P. Oliveira, R.F. Nascimento, A.R. Loiola, Al-MCM-41 synthesized from kaolin via hydrothermal route: structural characterization and use as an efficient adsorbent of methylene blue, J. Braz. Chem. Soc., 29 (2018) 2378–2386.

[20] K. Vikrant, K.-H. Kim, J.E. Szulejko, The retrograde adsorption phenomenon at the onset of breakthrough and its quantitation: an experimental case study for gaseous toluene on activated carbon surface, Environ. Res., 178 (2019) 108737, doi: 10.1016/j.envres.2019.108737.

[21] L. Huang, Q.L. Huang, H.N. Xiao, M. Eić, Effect of cationic template on the adsorption of aromatic compounds in MCM-41, Microporous Mesoporous Mater., 98 (2007) 330–338.

[22] E. Amdeha, R.S. Mohamed, A green synthesized recyclable ZnO/MIL-101(Fe) for Rhodamine B dye removal via adsorption and photo-degradation under UV and visible light irradiation, Environ. Technol., 42 (2019) 842–859, doi: 10.1080/09593330.2019.1647290.

[23] H.M. Gobara, R.S. Mohamed, S.A. Hassan, F.H. Khalil, M.S. El-Sall, Pt and Ni nanoparticles anchored into metal–organic frameworks MIL-101 (Cr) as swift catalysts for ethanol dehydration, Catal. Lett., 146 (2016) 1875–1885.

[24] H.M. Gobara, S.A. Hassan, A.M.A. El Naggar, R.S. Mohamed, A.A. Alkahlawy, A.A. Salem, H.M. Salem, Anomalous behavior of H_2 storage in photocatalytic splitting of water over Fe nanoparticles loaded on Al-modified SBA-15 composites via microwave or ultrasonic treatment routes, Int. J. Hydrogen Energy, 45 (2020) 24710–24725.

[25] R. Serna-Guerrero, A. Sayari, Applications of pore-expanded mesoporous silica. 7. adsorption of volatile organic compounds, Environ. Sci. Technol., 41 (2007) 4761–4766.

[26] Y.S. Liu, Z.Y. Li, X. Yang, Y. Xing, C.J. Tsai, Q. Yang, Z.Y. Wang, Performance of mesoporous silicas (MCM-41 and SBA-15) and carbon (CMK-3) in the removal of gas-phase naphthalene: adsorption capacity, rate and regenerability, RSC Adv., 6 (2016) 21193–21203.

[27] W.Z. Xu, G.S. Wang, Y.C. Liu, R. Chen, W. Li, Zeolitic imidazolate framework-8 was coated with silica and investigated as a flame retardant to improve the flame retardancy and smoke suppression of epoxy resin, RSC Adv., 8 (2018) 2575–2585.

[28] M. Sarker, J.Y. Song, S.H. Jhung, Adsorptive removal of anti-inflammatory drugs from water using graphene oxide/metal-organic framework composites, Chem. Eng. J., 335 (2018) 74–81.

[29] A. Kondo, S. Takanashi, K. Maeda, New insight into mesoporous silica for nano metal-organic framework, J. Colloid Interface Sci., 384 (2012) 110–115.

[30] S.Z. Li, F.W. Huo, Metal–organic framework composites: from fundamentals to applications, Nanoscale, 7 (2015) 7482–7501.

[31] Y.C. Pan, Y.Y. Liu, G.F. Zeng, L. Zhao, Z.P. Lai, Rapid synthesis of zeolitic imidazolate framework-8 (ZIF-8) nanocrystals in an aqueous system, Chem. Commun., 47 (2011) 2071–2073.

[32] C. Chen, B.X. Li, L.J. Zhou, Z.F. Xia, N.J. Feng, J. Ding, L. Wang, H. Wan, G.F. Guan, Synthesis of hierarchically structured hybrid materials by controlled self-assembly of metal–organic framework with mesoporous silica for CO_2 adsorption, ACS Appl. Mater. Interfaces, 9 (2017) 23060–23071.

[33] X.L. Yan, X.Y. Hu, S. Komarneni, Facile synthesis of mesoporous MOF/silica composites, RSC Adv., 4 (2014) 57501–57504.
[34] S.-H. Kim, J.-H. Park, Y. Hong, C.-Y. Lee, Removal of BTX using granular octyl-functionalized mesoporous silica nanoparticle, Int. Biodeterior. Biodegrad., 95 (2014) 219–224.
[35] X.L. Yan, Y.L. Yang, C. Wang, X.Y. Hu, M. Zhou, S. Komarneni, Synthesis of pore-expanded mesoporous ZIF-8/silica composites in the presence of swelling agent, J. Sol-Gel Sci. Technol., 81 (2017) 268–275.
[36] S.O. Akpotu, B. Moodley, Synthesis and characterization of citric acid grafted MCM-41 and its adsorption of cationic dyes, J. Environ. Chem. Eng., 4 (2016) 4503–4513.
[37] Y.H. Shu, Y.M. Shao, X.Y. Wei, X. Wang, Q.Q. Sun, Q.Y. Zhang, L.S. Li, Synthesis and characterization of Ni-MCM-41 for methyl blue adsorption, Microporous Mesoporous Mater., 214 (2015) 88–94.
[38] X.C. Xiao, F. Zhang, Z.P. Feng, S.J. Deng, Y.D. Wang, Adsorptive removal and kinetics of methylene blue from aqueous solution using NiO/MCM-41 composite, Physica E, 65 (2015) 4–12.
[39] X.W. Zhang, N. Huang, G. Wang, W.J. Dong, M. Yang, Y. Luan, Z. Shi, Synthesis of highly loaded and well dispersed CuO/SBA-15 via an ultrasonic post-grafting method and its application as a catalyst for the direct hydroxylation of benzene to phenol, Microporous Mesoporous Mater., 177 (2013) 47–53.
[40] H.M. Salem, R.S. Mohamed, A.A. Alkahlawy, H.M. Gobara, A.E.A. Hassan, S.A. Hassan, Enhanced ethylene production by dehydration of ethanol over Al/SBA-15 mesoporous catalysts, J. Porous Mater., 26 (2019) 735–745.
[41] Z. Mu, J.J. Li, Z.P. Hao, S.Z. Qiao, Direct synthesis of lanthanide-containing SBA-15 under weak acidic conditions and its catalytic study, Microporous Mesoporous Mater., 113 (2008) 72–80.
[42] S. Jatta, S.Y. Huang, C.J. Liang, A column study of persulfate chemical oxidative regeneration of toluene gas saturated activated carbon, Chem. Eng. J., 375 (2019) 122034, doi: 10.1016/j.cej.2019.122034.
[43] M. Fathy, M.A. Mousa, T.H.A. Moghny, A.-H.A.A. El-Bellihi, A.E. Awadallah, Novel amorphous carbon thin film (ACTF) from rice straw to remove sodium ions from synthetic saline water, Adv. Recycl. Waste Manage., 1 (2016), doi: 10.4172/2475-7675.1000111.
[44] R. Hosny, M. Fathy, O.H. Abdelraheem, M.A. Zayed, Utilization of cross-linked chitosan/ACTF biocomposite for softening hard water: optimization by adsorption modeling, Egypt. J. Chem., 63 (2020) 437–456.
[45] D. Fairen-Jimenez, S.A. Moggach, M.T. Wharmby, P.A. Wright, S. Parsons, T. Düren, Opening the gate: framework flexibility in ZIF-8 explored by experiments and simulations, J. Am. Chem. Soc., 133 (2011) 8900–8902.
[46] A. Jamal Sisi, M. Fathinia, A. Khataee, Y. Orooji, Systematic activation of potassium peroxydisulfate with ZIF-8 via sono-assisted catalytic process: mechanism and ecotoxicological analysis, J. Mol. Liq., 308 (2020) 113018, doi: 10.1016/j.molliq.2020.113018.
[47] A. Korus, A. Samson, A. Szlęk, A. Katelbach-Woźniak, S. Sładek, Pyrolytic toluene conversion to benzene and coke over activated carbon in a fixed-bed reactor, Fuel, 207 (2017) 283–292.
[48] X.R. Tian, B. Wu, J. Li, The exploration of making acidproof fracturing proppants using red mud, J. Hazard. Mater., 160 (2008) 589–593.
[49] S.M. Alardhi, T.M. Albayati, J.M. Alrubaye, Adsorption of the methyl green dye pollutant from aqueous solution using mesoporous materials MCM-41 in a fixed-bed column, Heliyon, 6 (2020) e03253, doi: 10.1016/j.heliyon.2020.e03253.
[50] G.D. Mihai, V. Meynen, M. Mertens, N. Bilba, P. Cool, E.F. Vansant, ZnO nanoparticles supported on mesoporous MCM-41 and SBA-15: a comparative physicochemical and photocatalytic study, J. Mater. Sci., 45 (2010) 5786–5794.
[51] C.M. Chen, X. Yan, B.A. Yoza, T.T. Zhou, Y. Li, Y. Zhan, Q.H. Wang, Q.X. Li, Efficiencies and mechanisms of ZSM5 zeolites loaded with cerium, iron, or manganese oxides for catalytic ozonation of nitrobenzene in water, Sci. Total Environ., 612 (2018) 1424–1432.
[52] H.H. Chen, H.P. Zhang, Y. Yan, Adsorption dynamics of toluene in structured fixed bed with ZSM-5 membrane/PSSF composites, Chem. Eng. J., 228 (2013) 336–344.
[53] A.B. Hernández-Abreu, S. Álvarez-Torrellas, V.I. Águeda, M. Larriba, J.A. Delgado, P.A. Calvo, J. García, New insights from modelling and estimation of mass transfer parameters in fixed-bed adsorption of Bisphenol A onto carbon materials, J. Contam. Hydrol., 228 (2020) 103566, doi: 10.1016/j.jconhyd.2019.103566.
[54] A.A.M. Daifullah, B.S. Girgis, Impact of surface characteristics of activated carbon on adsorption of BTEX, Colloids Surf., A, 214 (2003) 181–193.
[55] T.A. Saleh, V.K. Gupta, Processing methods, characteristics and adsorption behavior of tire derived carbons: a review, Adv. Colloid Interface Sci., 211 (2014) 93–101.
[56] A. Dehghan, A.A. Mohammadi, M. Yousefi, A.A. Najafpoor, M. Shams, S. Rezania, Enhanced kinetic removal of ciprofloxacin onto metal-organic frameworks by sonication, process optimization and metal leaching study, Nanomaterials (Basel), 9 (2019) 1422, doi: 10.3390/nano9101422.
[57] S.K. Ghadiri, H. Alidadi, N. Tavakkoli Nezhad, A. Javid, A. Roudbari, S.S. Talebi, A.A. Mohammadi, M. Shams, S. Rezania, Valorization of biomass into amine- functionalized bio graphene for efficient ciprofloxacin adsorption in water-modeling and optimization study, PLoS One. 15 (2020) e0231045, doi: 10.1371/journal.pone.0231045.
[58] M. Yousefi, R. Nabizadeh, M. Alimohammadi, A.A. Mohammadi, A.H. Mahvi, Removal of phosphate from aqueous solutions using granular ferric hydroxide process optimization by response surface methodology, Desal. Water Treat., 158 (2019) 290–300.
[59] K.X. Xiao, H. Liu, Y. Li, G.Y. Yang, Y.J. Wang, H. Yao, Excellent performance of porous carbon from urea-assisted hydrochar of orange peel for toluene and iodine adsorption, Chem. Eng. J., 382 (2020) 122997, doi: 10.1016/j.cej.2019.122997.
[60] H.J. Bart, R. Germerdonk, P. Ning, Two-dimensional non-isothermal model for toluene adsorption in a fixed-bed adsorber, Chem. Eng. Process. Process Intensif., 35 (1996) 57–64.
[61] H.P. Zhang, C. Luo, Y. Yan, Adsorption dynamics of isopropanol in structured fixed bed with microfibrous ZSM-5 zeolite structured composite, J. Taiwan Inst. Chem. Eng., 80 (2017) 779–786.
[62] M.S. Hussein, M.J. Ahmed, Fixed bed and batch adsorption of benzene and toluene from aromatic hydrocarbons on 5A molecular sieve zeolite, Mater. Chem. Phys., 181 (2016) 512–517.
[63] D. Wang, E. McLaughlin, R. Pfeffer, Y.S. Lin, Aqueous phase adsorption of toluene in a packed and fluidized bed of hydrophobic aerogels, Chem. Eng. J., 168 (2011) 1201–1208.
[64] M. Basu, A.K. Guha, L. Ray, Adsorption of lead on lentil husk in fixed bed column bioreactor, Bioresour. Technol., 283 (2019) 86–95.
[65] M.A.E. de Franco, C.B. de Carvalho, M.M. Bonetto, R. de P. Soares, L.A. Féris, Removal of amoxicillin from water by adsorption onto activated carbon in batch process and fixed-bed column: kinetics, isotherms, experimental design and breakthrough curves modeling, J. Cleaner Prod., 161 (2017) 947–956.
[66] K.S. Rao, S. Anand, P. Venkateswarlu, Modeling the kinetics of Cd(II) adsorption on *Syzygium cumini* L leaf powder in a fixed bed mini-column, J. Ind. Eng. Chem., 17 (2011) 174–181.
[67] M.E. González-López, A.A. Pérez-Fonseca, M. Arellano, C. Gómez, J.R. Robledo-Ortíz, Fixed-bed adsorption of Cr(VI) onto chitosan supported on highly porous composites, Environ. Technol. Innov., 19 (2020) 100824, doi: 10.1016/j.eti.2020.100824.
[68] H. Jiang, Y. Yang, J. Yu, Application of concentration-dependent HSDM to the lithium adsorption from brine in fixed bed columns, Sep. Purif. Technol., 241 (2020) 116682, doi: 10.1016/j.seppur.2020.116682.
[69] J.X. Chen, K.L. Liu, M.H. Jiang, J. Han, M.L. Liu, C.B. Wang, C.L. Li, Controllable preparation of porous hollow carbon sphere@ZIF-8: novel core-shell nanomaterial for Pb^{2+} adsorption, Colloids Surf., A, 568 (2019) 461–469.

Supporting information

- The linearized form of the Thomas model is expressed as:

$$\ln\left(\frac{C_0}{C_t}-1\right)=\frac{k_{TH}q_e m}{Q}-k_{TH}C_0 t \quad (1)$$

where t is the flow time (min); C_0 is influent concentration (mg/L); C_t is effluent concentrations (mg/L); k_{TH} is the Thomas kinetic coefficient (mL/min mg); q_e is adsorption capacity (mg/g); m is mass of the adsorbent (g); Q is the volumetric flow rate (mL/min).

- The linearized Adams–Bohart equation is provided as:

$$\ln\left(\frac{C_0}{C_t}-1\right)=k_{AB}N_0\frac{Z}{F}-k_{AB}C_0 t \quad (2)$$

where t is the flow time (min); C_0 is influent concentration (mg/L); C_t is effluent concentrations (mg/L); k_{AB} is the Adams–Bohart kinetic constant (L/mg min); N_o is the saturation concentration (mg/L); Z is the bed depth of the fixed-bed column (cm); F is the superficial velocity (cm/min).

- The linearized the Yoon–Nelson model equation is provided as:

$$\ln\left(\frac{C_0}{C_t}-1\right)=\tau k_{YN}-k_{YN}t \quad (3)$$

where t is the flow time (min); C_0 is influent concentration (mg/L); C_t is effluent concentrations (mg/L); k_{YN} is the rate constant (min^{-1}); τ is the time required for 50% adsorbate breakthrough (min).

- All three kinetic models are regarded as mathematically equivalent and can be represented by a similar fitting equation:

$$\ln\left(\frac{C_0}{C_t}-1\right)=a-bt \quad (4)$$

where a represents $k_{TH}q_e m/Q$ (Thomas model), $k_{AB}N_o Z/F$ (Adams–Bohart model), and τk_{YN} (Yoon–Nelson model), while b is equivalent to $k_{TH}C_0$ (Thomas model), $k_{AB}C_0$ (Adams–Bohart model), and k_{YN} (Yoon–Nelson model).